Zero-Emission Multivalorization of Light Alcohols with Self-Separable Pure H_2 Fuel

Nasir Uddin[1], Julien Langley[1], Dr. Chao Zhang [2, 3], Alfred K. K. Fung[1], Dr. Haijao Lu[1], Dr. Xinmao Yin [4, 5], Dr. Jingying Liu [6], Zhichen Wan [6], Dr. Hieu T. Nguyen [7], Dr. Yunguo Li[8], Dr. Nicholas Cox[1], Prof. Andrew T. S. Wee [4, 5], Prof. Qiaoling Bao [6], Dr. Shibo Xi [9], Prof. Dmitri Golberg [2,3,10], Prof. Michelle L. Coote [1] & Dr. Zongyou Yin[1*]

[1]Research School of Chemistry, Australian National University, ACT 2601, Australia

[2]Centre for Materials Science, Queensland University of Technology (QUT), 2 George Street, Brisbane, Queensland 4000, Australia

[3]School of Chemistry and Physics, Science and Engineering Faculty, Queensland University of Technology (QUT), 2 George Street, Brisbane, Queensland 4000, Australia

[4]Department of Physics, Faculty of Science, National University of Singapore, Singapore 117542, Singapore

[5]Singapore Synchrotron Light Source (SSLS), National University of Singapore, Singapore 117603, Singapore

[6]Department of Materials Science and Engineering, Monash University, Clayton, Victoria 3800, Australia

[7]Research School of Electrical, Energy and Materials Engineering, Australian National University, ACT 2601, Australia

[8]Faculty of Mathematical and Physical Sciences, University College London, Gower Street, London WC1E 6BT, United Kingdom

[9]Institute of Chemical and Engineering Sciences, A*STAR, 1 Pesek Road, Jurong Island, 627833 Singapore

[10]International Centre for Materials Nanoarchitectonics (MANA), National Institute for Materials Science (NIMS), 1-1 Namiki, Tsukuba, Ibaraki 305-0044, Japan

[*]Corresponding authors. Email: zongyou.yin@anu.edu.au; michelle.coote@anu.edu.au

ABSTRACT

To reach Paris Agreement's target of 1.5 °C global temperature increase by 2100, low emission strategies are crucial. In synthetic chemistry, the phototransformation of light alcohols (methanol, ethanol and iso-propanol) into hydrogen fuel and chemicals promises high potential utility value for industry. However, this process is often practiced using promoters (i.e. water, acid or base), with and several issues remained unsolved, e.g. water promoter induce CO_2 emission; acid/base promoters restrict catalyst selection, and lead to complicated product purification and cost increase. In this work, we report solar-driven promoter-free multivalorization of light alcohols into self-separable hydrogen gas/fuel and liquid chemicals without CO_x emission based on the two-dimensional (2D) SnS/g-C_3N_4 heterojunction. The hydrogen production efficiency reaches 1.27 $mmol.g^{-1}.h^{-1}$ with ~ 95% recoverability. The process reduction occurs via a sequence of redox reactions, combination and disproportionation, as confirmed from experimental and product analysis. This work demonstrates the effectiveness of 2D heterojunctions for promoter-free, zero-emission alcohol phototransformations.

KEYWORDS: zero emission，selective phototransformation，stable performance, 2D heterojunctions, multivalorization, light alcohol

1. INTRODUCTION

The Paris Agreement on Climate Change targets at 1.5 °C global temperature increase by 2100. To reach this target, it is imperative to deploy the sustainable strategies, i.e. both to reduce anthropogenic emissions in related sectors towards zero level and also capture CO_2 from the atmosphere for negative emissions.[1-5] As an essential source of renewable energy, solar energy annually intercepted by our Planet can reach ~ 49,800 exajoules, which is over 25 times higher than the projected global primary energy consumption (1,900 exajoules) in year 2100.[6] However, our utilization of solar energy still needs huge improvement as seen from this fact: the most matured solar photovoltaics (PV) only supplies 2.8% of the global electricity production in 2019.[7] With world population and human activities forecast to increase, it is of vital importance to diversify solar harnessing methods beyond solar PV. [8]

One such promising zero-emission technology is the phototransformation of light alcohols (PTLAs), such as methanol, ethanol and iso-propanol, etc., in hydrogen fuel and useful chemical feedstocks. Generally, the PTLAs involves dehydrogenation steps that convert LAs into clean hydrogen fuel for fuel cells, and carbonyl compounds (e.g. aldehydes, ketones, and/or carboxylic acids, etc.) for producing wide varieties of organic compounds with applications including as fragrances, food, agrochemicals, materials and pharmaceuticals, etc.[9] To date studies on H_2 fuel production from LAs typically use promoters (e.g., water [10-14], acid [15-17], and base [18-19]). Promoters benefit catalytic reactions, but there still remain problems: water promoter based reactions emit CO_2; and acid/base promoters limit catalyst selection, and lead to complicated product purification and cost increase. [16, 20] Promoter-free strategies for PTLAs are thus becoming increasingly attractive.

While promoter-free strategies have been developed, some issues remain, such as greenhouse gases emissions [21-24], reliance on noble metals [25-28], and the requirement for full UV light irradiation.[29] Recently, our group made a breakthrough by overcoming the above issues using

monocomponent MoS_2. However, the short lifetime of the carriers restricted H_2 production efficiency (617 $\mu mol\ h^{-1}\ g^{-1}$), and generated gaseous formaldehyde. This in turn needs ~ 5 atm pressure to be liquefied, thus complicating product (H_2-formaldyhyde) separation.[30]

This has inspired us to explore new strategies to address above combined challenges. As a widely applied 2D semiconductor photocatalyst, graphitic carbon nitride (g-C_3N_4) is based on abundant elements, and has excellent photochemical stability, a visible light responsive bandgap (~ 2.7 eV), and Lewis and Brönsted basic functions. [31-34] The noble-metal free SnS also tends to form 2D structures but has a near infrared bandgap, complementing g-C_3N_4.[35] Taking advantage of these properties, a 2D/2D heterojunction between g-C_3N_4 and SnS is first developed to evaluate the performance of PTLAs for photocatalytic alcohol to self-separable hydrogen (PATH) and valuable chemicals. The characteristics and catalytic behaviour of 2D SnS/g-C_3N_4 are then elucidated in detail, and the reaction mechanism explored.

2. RESULTS AND DISCUSSION

2.1. Materials Characterization

Powder X-ray powder diffraction (XRD) analysis was performed to reveal the nature of the crystallinity of the materials prepared (see Method section for full details) in this work. In Figure 1a, the characteristic peak associated with g-C_3N_4 can be observed at $2\theta = 27.78^o$, which has been reported as the (002) plane with a d-spacing of 0.32 nm. [36] This can be ascribed to the interlayer stacking of the conjugated aromatic system. The crystal structure analysis reveals that the SnS appeared with multiple peaks, consistent with previous studies on SnS. [37] After forming a heterojunction with 2D g-C_3N_4 nanosheets (see Note S1, Figure S1a), SnS retains its all feature peaks with one new peak at $2\theta = 27.78^o$ which is from (002) planes of g-C_3N_4. This indicates that 2D g-C_3N_4 was successfully integrated with SnS without shifting the positions of characteristic diffraction peaks.

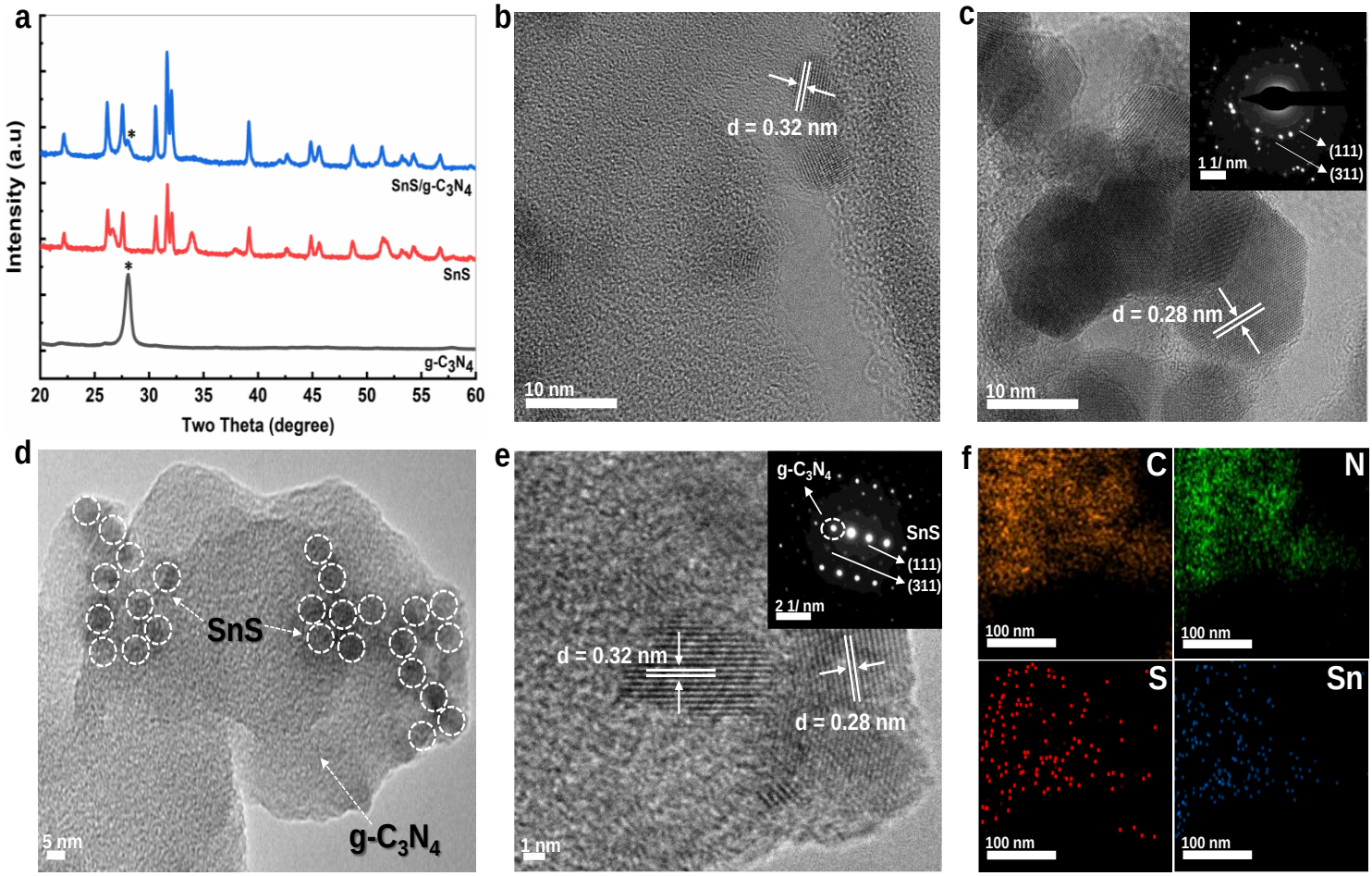

Figure 1. Powder XRD, high-resolution transmission electron microscopy (HRTEM) images, and Selected Area Electron Diffraction (SAED) results of SnS, and SnS/g-C_3N_4 and EDS spatially-resolved elemental maps for SnS/g-C_3N_4 heterojunction. (a) XRD patterns of different catalysts. "*" symbol represents (002) plane of g-C_3N_4 sample. (b) HR-TEM image of g-C_3N_4. (c) HR-TEM image of SnS. Inset in (c) is the SAED pattern of SnS. (d) and (e) are the HR-TEM images of SnS/g-C_3N_4. The dotted white circle represents SnS in d. Inset in (e) is the SAED pattern of SnS/g-C_3N_4 catalysts. (f) Scanning transmission electron microscopy-energy dispersive X-ray spectroscopy (STEM-EDS) elemental map shows co-existence of C, N, S, and Sn in SnS/g-C_3N_4 heterostructure.

High-resolution transmission electron microscopy (HRTEM) was performed to study the prepared materials. In Figure 1b, the lattice fringes separated by a c.a. 0.32 nm distance can be ascribed to the (002) plane of g-C_3N_4 nanosheets. A layered SnS (orthorhombic) (see Figure

S1b) phase with interplanar d-spacing of c.a. 0.28 nm was observed in Figure 1c, which can be attributed to the (111) plane d-spacing of SnS. The SAED pattern (inset in Figure 1c) reveals the polycrystalline nature of SnS, consistent with XRD results, while representing some larger grains with preferred orientation. Additionally, SnS nanosheets have a lateral size of up to tens of nanometers. The TEM image of SnS/g-C_3N_4 heterostructures shows that SnS nanosheets are randomly and tightly anchored near the edges of g-C_3N_4 sheets (Figure 1d). Both HRTEM image and SAED pattern confirm that the heterostructures consist of both SnS and g-C_3N_4 components (Figure S1c), as evidenced by the characteristic interplanar distances of 0.32 nm and 0.28 nm corresponding to (002) planes of g-C_3N_4 and (111) planes of SnS, respectively, (Figure 1e and its inset). STEM-EDX elemental mapping verifies the co-existence and indicates the spatial distribution of C, N, S, and Sn species in the heterostructures, as shown in Figure 1f.

X-ray photoelectron spectroscopy (XPS) was performed to obtain surface chemical states of the photocatalysts. The survey spectrum of SnS/g-C_3N_4 heterojunction shows the signals of S, Sn, C, and N elements (Figure S2), indicating their coexistence. Seen from Figure 2a, the binding energies of Sn $3d_{5/2}$ and $3d_{3/2}$ in SnS/g-C_3N_4 were shifted to 486.23 eV and 494.45 eV compared with those of 486.81 eV and 495.10 eV in SnS, respectively. The binding energies of these two orbitals can be ascribed to the Sn^{2+}, providing evidence for the existence of SnS, and their small shifts in SnS/g-C_3N_4 compared with SnS suggest some interactions between the SnS and g-C_3N_4 nanosheets.[38-39] The S 2p spectrum is a doublet (Figure 2b) representing the spin-orbit splitting of the S $2p_{3/2}$ (S^{2-} phase) and S $2p_{1/2}$ lines (S^{2-} phase), while observing minor S^o impurities.[40] After forming the heterojunction, both the peaks of S $2p_{3/2}$ and S $2p_{1/2}$ shifted to lower binding energies around 161.44 and 162.64 eV, respectively, which, however, represents the monosulfide phase of the surface.[41] As shown in Figure 2c, the deconvolution of C 1s peak generates characteristic peaks at 288.20 and 284.44 eV ascribed to the sp^2-bonded

C atom bonded to N within the *s-triazine* ring (N-C=N) and sp^2 C–C in graphitic carbon, respectively, while the weak peak at 286.20 eV indicates possible surface oxidation of carbon (for example C-O).[42] It is likely that the synthesis of g-C_3N_4 plays a role in this oxidation. After forming the heterostructure, the peak intensities of N-C=N bonds undergo a slight energy reduction to 288.14 eV, indicating the nature of highly ordered g-C_3N_4 nanosheets.[42] A new peak at 285.90 eV with a marginal height is observed, which could be attributed to a higher oxidization state of C atoms in C-O bonds. [42] In Figure 2d, the spectrum deconvolution of N 1s of pure g-C_3N_4 shows three peaks, which are attributed to sp^2-bonded nitrogen (N–C=N, 398.47 eV), a resonance form of the melamine structure involving –NH_2 group (400.95 eV) [43] and Π excitation of carbon atom (403.77 eV). [44] However, the peak at 401.1 eV is assigned to C-N-H uncondensed amino (-NH_2) groups, signalling the incomplete loss of NH_3 from melamine [42-43] while peak at 404.44 eV coincides with same Π excitation within the s-triazine. [43-44] The above XPS results are consistent with the XRD (Figure 1a) and FT-IR results (see Figure S3).

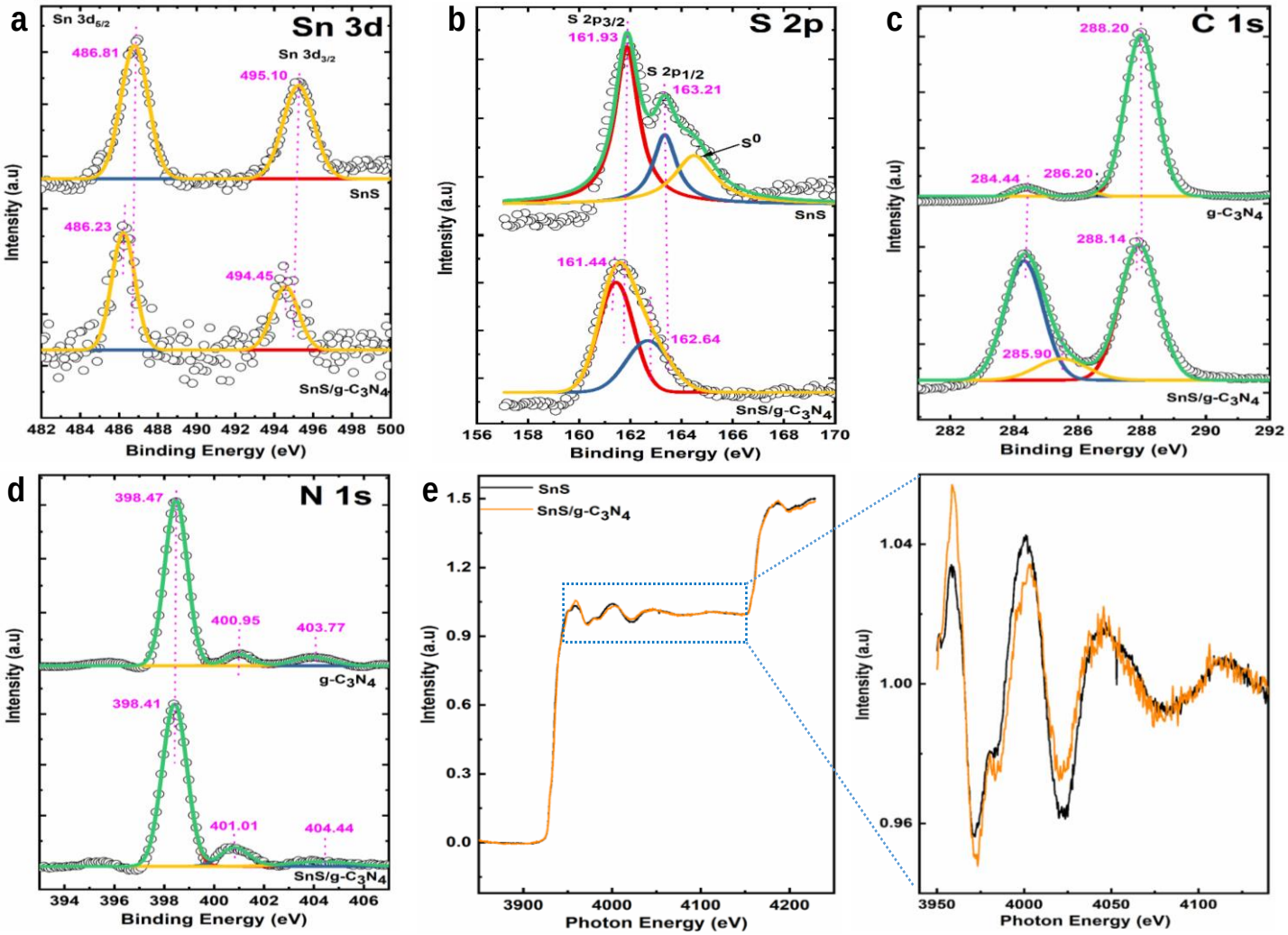

Figure 2. XPS and XAFS profiles of SnS and SnS/g-C_3N_4. (a) Sn 3d spectrum, (b) S 2p spectrum, (c) C 1s spectrum, and (d) N 1s spectrum. (e) Sn L_3 edge XAFS spectra of SnS and SnS/g-C_3N_4 catalysts. Zoom in areas of the dotted box, represents the spectra from photon energy 3925 to 4140 eV.

In order to investigate the electronic structure of the resulting SnS nanosheets on the g-C_3N_4 surface, X-ray absorption fine structure (XAFS) spectroscopy was performed for both SnS and SnS/g-C_3N_4 heterostructure. Theoretically, the L-edge XAFS spectra of Sn has L_1, L_2 and L_3 edges where L_1, L_2 and are ascribed to the transition of electrons from $2s_{1/2}$ to $np_{3/2}$, $2p_{1/2}$ to $nd_{3/2}$ and $2p_{3/2}$ to $nd_{5/2}$ states, respectively. [45] It is clearly evident from Figure 2e that there are a white line (~ 3955 eV) and some fine structures in the L_3-edge region. The zoom in figure

shows that the white line is significantly different before and after forming the heterojunction. [45] The peak intensities of the white line and the fine structures for SnS/g-C_3N_4 were significantly changed from those of SnS, associated with the electronic structure change after forming the heterojunction due to the presence of unoccupied 5d-symmetry orbitals in SnS. [45] By analysing the L_3 white line and the peak intensities for SnS and SnS/g-C_3N_4 heterojunction, it is revealed that there may be a strong interaction built up between SnS nanosheets and 2D g-C_3N_4 nanosheets.

2.2. Evaluation on PTLAs

A description of all operating parameters and their optimization in terms of PATH efficiency, including surfactant loadings, growth time, annealing temperature and pressure, catalyst dosage, effects of bare catalysts and heavier alcohols, and solar light intensity are optimized for SnS/g-C_3N_4 photocatalyst in terms of PATH efficiency (see Note S2, Figure S4a-e, Figure S5a, b, Figure S6a, b, Figure S7a, b, and Figure S8). After the optimization of the SnS/g-C_3N_4 photocatalyst in PTLAs, its stability was further examined for different alcohols by employing AM 1.5 G filter.

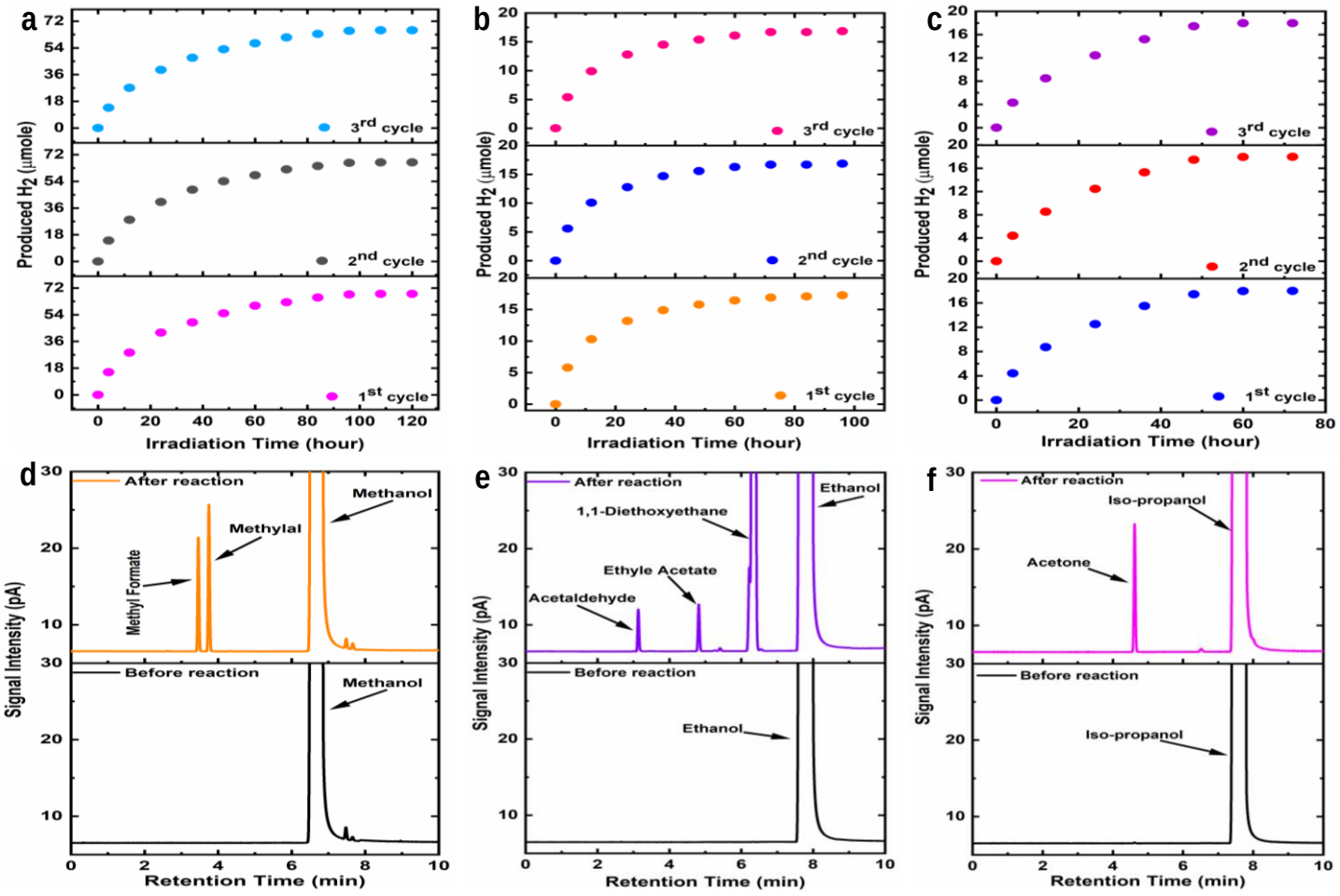

Figure 3. Representation of methanol, ethanol and iso-propanol stability test. (a) Methanol, (b) Ethanol, and (c) Iso-propanol. Identification of the end products from methanol, ethanol and – iso-propanol before and after reaction. (d, e, and f) are the gas chromatography-flame ionization detection (GC-FID) results of methanol, ethanol, and iso-propanol systems, respectively.

As seen from Figure 3a, the H_2 production increases over the irradiation time until reaches a plateau after 100 hours. This is because the produced H_2 inside the reactor will build up partial pressure and hence slow down methanol decomposition, and, the active sites of SnS/g-C_3N_4 may be partially blocked by the adsorption of evolved liquid products. After three cycles of experiment (120 hours for each cycle), about 1273.692, 1173.745, and 1140.358 μmole. g^{-1}. h^{-1} of H_2 was released from methanol in the 1st, 2nd and 3rd cycle, respectively (Table1), indicating

the PATH efficiency in the next cycle was as high as ~ 95% that of the previous cycle. These efficiencies are more than twice the reported values. [30] Taking methanol as a model PTLAs, the apparent quantum efficiency was calculated to be 5.78% while the solar to hydrogen efficiency (STH) conversion efficiency was around 2.46% (Note S3). Apart from methanol, ethanol can also be decomposed by SnS/g-C_3N_4 while it remains stable for 90 hours (Figure 3b). In a similar fashion, iso-propanol system was examined for H_2 formation whereas the stability test for iso-propanol is found to be relatively shorter (72 hours) than those of methanol and ethanol test (Figure 3c). This is because the in-situ produced acetone may experience hydrogenation, reducing the H_2 generation further. [46] The initial and specific reaction rates for photo-redox induced methanol, ethanol, and iso-propanol systems were also determined using the n^{th} order polynomial fit for each cycle (Table 1).

Table 1. Estimated H_2 efficiency, initial and specific reaction rates for PTLAs system.

Photo-redox system	**H_2 efficiency[a] ($\mu mole.g^{-1}.h^{-1}$)**			**Initial reaction rate[b] ($\mu mole.\ s^{-1}$) × 10^{-4}**			**Specific reaction rate[c] ($\mu mole.g^{-1}.s^{-1}$)**		
	1^{st} cycle	2^{nd} cycle	3^{rd} cycle	1^{st} cycle	2^{nd} cycle	3^{rd} cycle	1^{st} cycle	2^{nd} cycle	3^{rd} cycle
Methanol	1273.692	1173.745	1140.358	8.79	8.52	8.19	0.293	0.284	0.273
Ethanol	481.948	465.282	448.615	3.75	3.66	3.6	0.125	0.122	0.120
Iso-propanol	368.60	365.30	358.60	3.41	3.35	3.31	0.113	0.111	0.110

Note: "a" Hydrogen efficiency was derived from Figure S9a-c.

"b" Initial hydrogen rate was calculated by using the n^{th} order polynomial equation with $R^2 >$ 0.99 and then substituted of the time variables at zero into the right hand side of the curve fitting equation using Figure 3 a, b, and c for methanol (Figure S10), ethanol (Figure S11) and iso-propanol (Figure S12), respectively.

"c" Specific reaction rate was calculated from the ratio of initial hydrogen rate and amount of used catalysts for particular reaction system (Note S2).

Clearly, Table 1 shows that the photocatalytic performance can be maintained at about 95% in the subsequent cycle for all the three light alcohols, and the initial and specific reaction rates enabled by photo-excitation are in close proximity for each PTLAs. All these consistently demonstrated reaction reversibility using 2D SnS/g-C_3N_4 heterojunction. Importantly, the stability of SnS/g-C_3N_4 heterojunction before and after PTLAs reactions was verified using the powder XRD patterns, which showing same characteristic peaks (Note S4, Figure S13a). This can be further co-supported by excellent thermos-stability even under 450 °C (Figure S13b). More importantly, the ultra-efficient PTLAs to hydrogen conversion over SnS/g-C_3N_4 heterojunction has an extra advantage over traditional thermos-catalytic processes [47-49] since it is still completely free from CO_x side-products (Note S5, Figure S14 and S15). The liquid-phase products were investigated by GC-FID and gas-chromatography tandem mass spectroscopy (GC/MS/MS) (Note S6, Figures S16-21). Methylal and methyl formate (MF) appeared after methanol decomposition in Figure 3d, and 1, 1-diethoxyethane (DEE), ethyl acetate (EA), and acetaldehyde emerged after ethanol decomposition in Figure 3e. The scenario for iso-propanol was simpler, showing only one peak assigned to acetone (Figure 3f). However, among the liquid products, the selectivity, or product distribution, of producing methylal and MF was calculated to be 54.28 and 45.71 %, respectively, over methanol photodecomposition, wherein 95.59, 2.38 and 2.01 % for DEE, EA and acetaldehyde in ethanol system, respectively. Evidently, with the SnS/g-C_3N_4 heterojunction in this work, the reaction pathways and resultant products are different from the previous works where the gaseous formaldehyde was consistently observed in methanol photodecomposition. [29-30] Compared with gaseous formaldehyde, our received liquid methylal and MF can be easily separated from H_2 fuel. Furthermore, the ethanol decomposition shows a much higher selectivity of DEE over the

acetaldehyde formation, and only one main product of acetone (100% selectivity) was generated from iso-propanol (Figures S16-21). All these provide evidence that the employed SnS/g-C_3N_4 heterojunction can multivalorize LAs by selectively generating a wide category of valuable liquid chemicals with H_2 fuel.

2.3. SnS/g-C_3N_4 Z-scheme heterojunction enabled photoredox activities

Among electrochemical impedance spectroscopy, Nyquist plots can describe the nature of charge transfer across the SnS/g-C_3N_4 heterojunction. As is seen from Figure 4a, the curvature radius of the composite is much smaller than that of pure g-C_3N_4 and SnS. This implies that the SnS/g-C_3N_4 heterojunction effectively improves charge carrier transport after separation. Mott-Scottky analysis was performed to provide insight into the band structures of g-C_3N_4 and SnS as shown in Figure 4b. The Mott-Scottky plot of SnS shows a negative slope, suggesting its p-type nature, while that of g-C_3N_4 has a positive slope, which indicates an n-type semiconductor. [50] The flat band potentials can be estimated from the x-axis intercepts of the linear region, with values of 1.45 V and -1.58 V (vs Ag/AgCl) obtained for SnS and g-C_3N_4, respectively. [51] Using the bandgap (Note S7, Figure S22) and Mott-Schottky data, the potential Z-scheme band diagram was plotted as shown in Figure 4c. It is known that charge carriers can easily transfer across the interfaces and the recombination/coupling between electrons from SnS and holes from g-C_3N_4 is greatly enhanced in Z-scheme heterojunction [52], which benefit the electron-hole separations for both SnS and g-C_3N_4, thus substantially extending the lifetime of both electrons@g-C_3N_4 and holes@SnS. The electron-hole separation of SnS/g-C_3N_4 heterojunction was significantly improved compared with that of pure g-C_3N_4, which was verified by the dramatically decreased (~100 times) photoluminescence intensity of g-C_3N_4 after forming heterojunction (Figure 4d). [41] The spatially-separated longer-lifetime electrons at conduction band of g-C_3N_4 and holes at valence band of SnS directly improved heterojunction's PATH performance, compared with single components (SnS or g-C_3N_4), and

also modified reaction pathways during PTLAs. It is worth highlighting here that the above mentioned p-type SnS and n-type g-C_3N_4 forms a Z-scheme heterojunction instead of a conventional p-n heterojunction. [33, 53]. The reason is that the electrons tend to remain at g-C_3N_4 and holes stay at SnS, thus forming a direct Z-scheme junction, and no depletion region exists in the atomically thin area to form a p-n heterojunction. [33, 53]

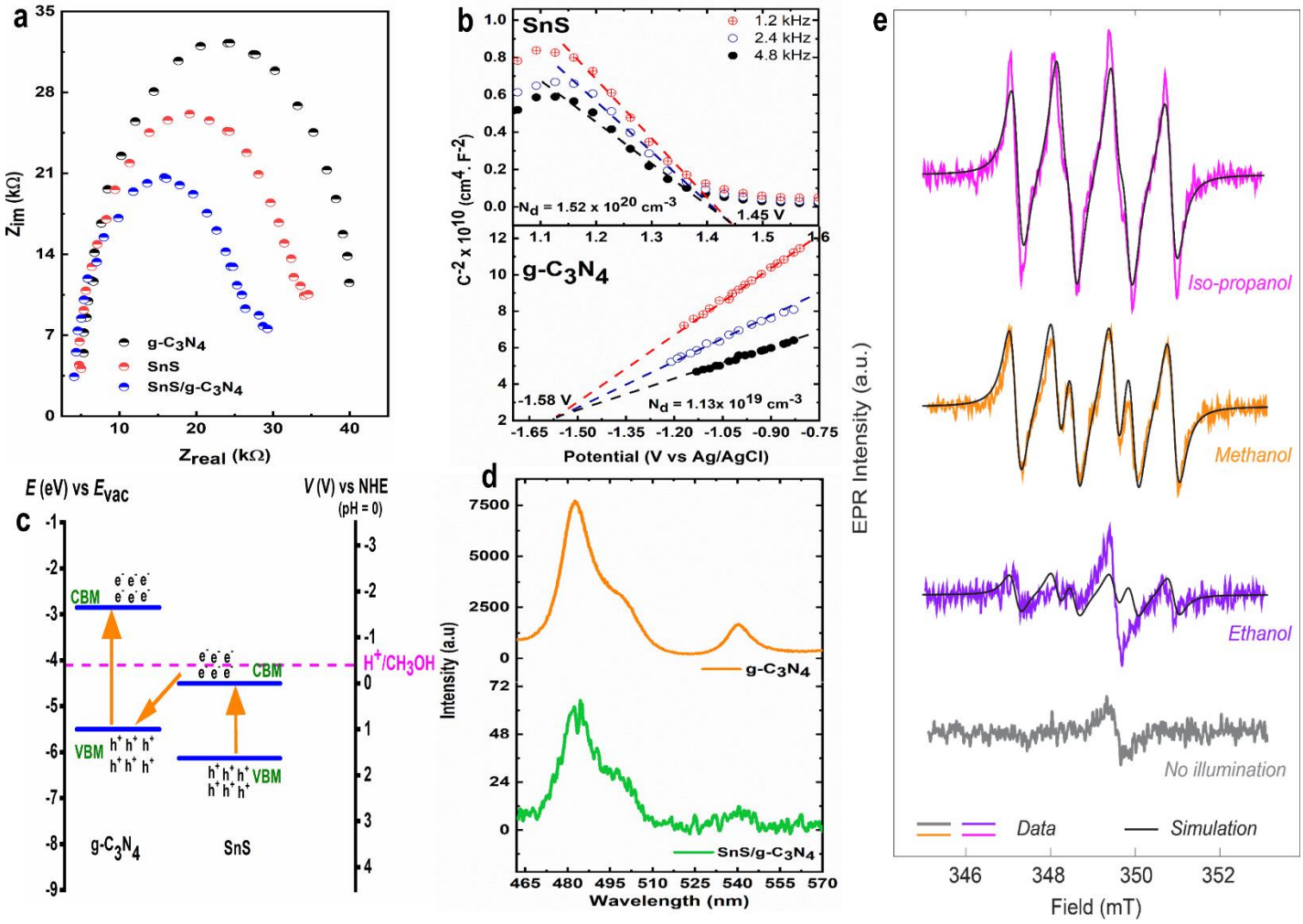

Figure 4. Schematic representation of EIS for (a) g-C_3N_4, SnS, and SnS/g-C_3N_4, (b) Mott-Schottky plots for SnS and g-C_3N_4, (c) Z-scheme band diagram for SnS/g-C_3N_4 heterojunction for methanol system, (d) PL spectra for g-C_3N_4, and SnS/g-C_3N_4 heterostructure, and (e) Electron paramagnetic resonance (EPR) measurements to identify the free radicals. CW X-Band EPR of 150 mM DMPO – ethanol (purple), methanol (orange) and iso-propanol (pink)

reaction mixtures post illumination and prior to illumination (grey). The derivative signal that is present prior to illumination is assigned to SnS/g-C_3N_4 heterostructure. Spin-Hamiltonian simulations are superimposed (black). [54] Fitted hyperfine coupling constants were: a_N (14.1), a_H (9.6) for methanol, a_N (13.9), a_H (9.6) for ethanol, and a_N (13), a_H (10.4) for iso-propanol, respectively.

Besides carrier lifetime extension, the Z-scheme heterojunction can also widen the spatial separation of reductive/oxidative energy levels of photoexcited electrons/holes so as to possess high redox capacities. [55] In this work, high oxidative capacity over the Z-scheme structure was investigated by EPR, where the free radical intermediates during the PLTAs were studied, as shown in Figure 4e. In presence of 5, 5-Dimethyl-1-Pyrroline-N-Oxide (DMPO) spin trap, oxygen centered radical intermediates such as $CH_3O^{\bullet}$, $CH_3CH_2O^{\bullet}$, and $(CH_3)_2CHO^{\bullet}$ were detected, for methanol, ethanol and iso-propanol, respectively. Radical yields were highest for iso-propanol and methanol. These short-lived intermediates were also captured as fragmented molecules in GC-MS-MS experiments (Figures S16-21). Based on the above analyses, it is inferred that the abovementioned free radical intermediates were generated from the alcohol molecules through the oxidization by photoexcited holes from valence band of SnS. These intermediates will be further transformed into carbon-centered radical which undergoes combination/disproportionation reaction to form the specific liquid products as discussed in next section. Meanwhile, the liberated protons from alcohol molecules were reduced to H_2 by accepting the electrons from conduction band of g-C_3N_4.

2.4. Reaction mechanism

The mechanism of methanol photooxidation (Scheme 1) has been described previously. [56] It begins with the photoexcitation of the catalyst, upon which it undergoes an electron transfer reaction with methanol. [30] The resulting methanol radical cation readily deprotonates to afford the methoxy radical, which can then undergo further reaction. [57-58] The catalyst is regenerated

by a further electron transfer reaction with the proton to afford hydrogen. The methoxy radical ($CH_3O^{\bullet}$) readily undergoes a 1, 2 intramolecular hydrogen atom transfer to form the more stable carbon-centered radical. [59] In the absence of oxygen or other reagents, the only radical sinks are hydrogen atom transfer with methanol, a null reaction, or bimolecular radical termination. Termination can occur in two ways: the carbon centered radical can combine with the original methoxy radical to afford a hydroxy ether (A in Scheme 1), or it can undergo combination or disproportion with another carbon-centered radical. In this latter case, disproportion is favoured for steric reasons and leads to production of formaldehyde (B in Scheme 1) and methanol (starting material). The resulting products can then undergo further reactions. Specifically, the hydroxy ether A can either react with further methanol via the Tishchenko Reaction [60] to afford methylal (C in Scheme 1), or it can react with the acetaldehyde B via standard aldehyde protection chemistry [61] to afford methyl formate (D in Scheme 1) and methanol (starting material). Product analysis shows that only methylal and methyl formate are observed in similar amounts, which is consistent with the initial generation of both A and B, both of which react further to form C and D.

For higher alcohols, ethanol and iso-propanol, the same basic reaction scheme is possible, although the product ratios differ. Specifically, the reactivity of B declines with increasing substitution to the extent that in the case of iso-propanol, B is a ketone rather than an aldehyde and formation of D is impossible. For ethanol, some ethyl formate (D) is formed but unreacted acetaldehyde (B) is also observed, and the major product is thus 1, 1-diethoxyethane (C). Additionally, the relative populations of the oxygen and carbon-centred radical tautomers increasingly favours the carbon-centred radical as it becomes more substituted, and hence more stabilized. This, along with increasing steric hindrance, results in decreasing cross-termination between the oxygen and carbon centred radicals (and hence decreasing formation of A and

products derived from A), in favour of the disproportionation products (i.e. B), which in the case of iso-propanol are formed exclusively.

Scheme 1. Photooxidation of Methanol, Ethanol and Iso-propanol, together with experimental product ratios.

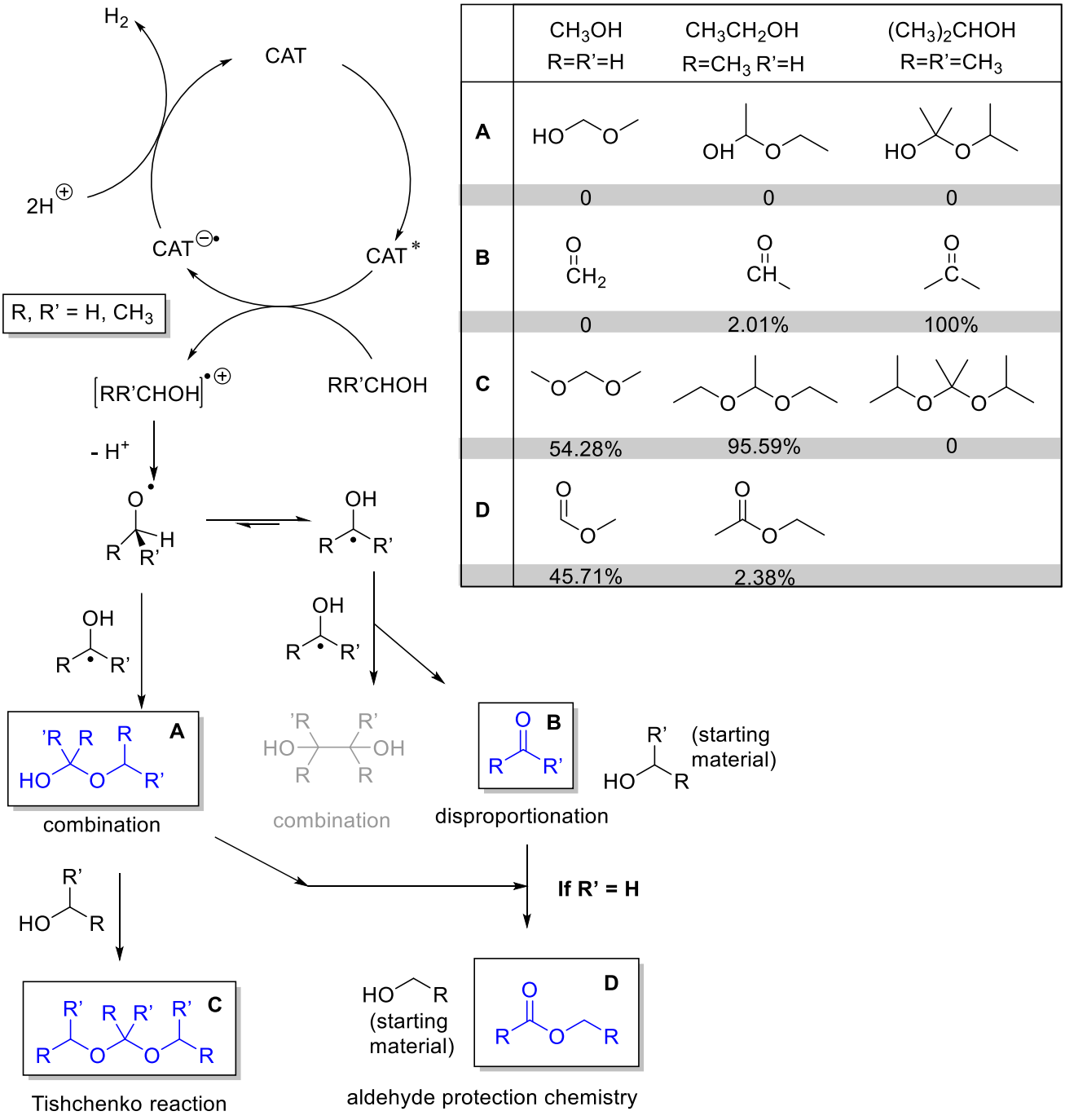

	CH_3OH R=R'=H	CH_3CH_2OH R=CH_3 R'=H	$(CH_3)_2CHOH$ R=R'=CH_3
A			
	0	0	0
B			
	0	2.01%	100%
C			
	54.28%	95.59%	0
D			
	45.71%	2.38%	

3. CONCLUSION

In this work, we show that 2D SnS/g-C_3N_4 heterostructures exhibit ultra-efficient and -stable phototransformation of light alcohols without any promoter at room temperature and free from CO_x by-products. The multivalorized products, i.e. H_2 fuel and liquid products, are easily self-separable. The hydrogen production efficiency from each studied alcohol exceeds the corresponding reported values whereas and furthermore is demonstrated excellent reversibility (>95%) during long-term operations (up to 360 hours in total). The mechanism was proposed based on reactive intermediates, derivative products and products selectivities. The phototransformation of light alcohols by 2D SnS/g-C_3N_4 heterostructures in this work exemplifies selective reaction pathways, where the unreactive alcohols can be activated as intermediates, for further combination/disproportionation towards valued liquid products. Some key advantages of this work: (i) mutivalorization of PTLAs into self-separable H_2 fuel and liquid products; (ii) greater utilization of H elements from alcohol molecules for high H_2 production efficiency with excellent reversibility; (iii) selective redox reactions to avoid CO_x formation; and (iv) in-situ combination/disproportionation of carbonyl products into higher value-added liquid chemicals. This work will advance the existing understanding of the selective roles of photoexcited electrons/holes in the heterojunction to attain the valuable fine products with zero emissions, and provide inspiration for the design of zero-emission catalysts with high product selectivity for various solar-based applications.

4. EXPERIMENTAL SECTION

Chemicals

Melamine (99%), tin (ii) chloride ($SnCl_2$. $2H_2O$, 98%), thioacetamide (99%), and cetyl trimethylammonium bromide (CTAB, 98%) were purchased from Sigma Aldrich. Alcohols such as methanol (99.9%), ethanol (99.5%), iso-propanol (99.9%), 1, 2-propanediol (99.5%), 1, 3-propanediol (98%), 1-propanol (99.7%), and 1-butanol (99.8%) were purchased from Sigma Aldrich. Free radical spin trapping reagent 5, 5-Dimethyl-1-pyrroline N-oxide (DMPO, 97%) was bought from Sigma Aldrich. H_2 (99.999%), Ar (99.997%) and CO_2 (99.95%) were purchased from BOC gas, Australia.

Preparation of graphitic carbon nitride (g-C_3N_4) sample

A desired amount of melamine was placed in a crucible and heated the crucible in a furnace at 600 ºC for 4 hours with a ramping rate of 10 ºC/min. Grinding of the resultant products affords yellow powder of g-C_3N_4.

Synthesize of SnS/g-C_3N_4 photocatalysts

To prepare SnS/g-C_3N_4 photocatalysts, firstly, 0.5 grams of tin (ii) chloride and 0.19 grams of thioacetamide were added into 40 mL deionized (DI) water (18.2 Ωm) with varying amounts of surfactant CTAB. After a homogeneous solution was obtained, the desired amount of yellow colored g-C_3N_4 powder was mixed with this solution under continuous stirring at room temperature. The resultant suspension was then transferred into an autoclave followed by heating at 180 ºC for 24 hours. The resultant solid was collected after cooling down and subsequently cleaned by washing with DI water for three times followed by drying at 60 ºC for 12 hours. The obtained solid was further annealed at 400 ºC for 2 hours in argon under atmospheric pressure. After annealing, the final solid turned black and was used for all the experiments.

High-Resolution Transmission Electron Microscopy (HR-TEM) and Energy Dispersive X-ray (EDX) characterizations were performed on a 200 kV JEOL JEM 2100 HR-TEM at room temperature. Images were captured by a TVIPS TemCam-XF416 CMOS camera. Energy dispersive X-ray (EDX) elemental maps of the materials were acquired by an Oxford X-Max 80 mm2 silicon drift EDX detector.

Scanning Electron microscopy (SEM) was performed using a Zeiss Ultraplus analytical FESEM at Center for Advanced Microscopy, Australian National University. The samples were prepared with ethanol solution and deposited on Si substrate for SEM analysis.

UV-Vis measurement was conducted on Cintra 2020 (GBC scientific Equipment) using quartz cuvette as a sample container. A blank without sample was measured as background before testing the samples.

Powder X-ray diffraction measurement was done on a PANalytical Empyrean XRD using Cu Kα (λ=1.5406 Å) radiation with a generator voltage and current of 45 kV and 40 mA, respectively.

X-ray photoelectron spectroscopy (XPS) was performed on a Nexsa (ThermoFisher Scientific) spectrometer. The system work function was calibrated for each sample by setting the main line of the C 1s spectrum to 284.8 eV. Each high resolution spectrum was fitted with a Gaussian-Lorentzian (70%-30%) line shape using a Shirley background.

Electron paramagnetic resonance (EPR) measurement was done on a commercial Bruker E500 spectrometer equipped with an ER4122 SHQ resonator with the following parameters: 150 mW, 9.8 GHz light and 0.5 G modulation amplitude. Liquid solution EPR measurements were analysed using a quartz flat cell. For spin trap experiments, 3 mg of SnS/g-C_3N_4 samples was dispersed in 10 mL solvent (methanol/ethanol/iso-propanol), followed by solar illumination for 4 hours at room temperature. For each alcohol, the same procedure was

carried out to produce mutiple EPR spectra for average. A small volume of the illuminated solution was then mixed with a certain volume of DMPO aqueous solution (150 mM). The reaction mixture was then used for EPR measurement. For reference purpose, an aliquot of this mixture was taken prior to illumination and its EPR spectrum was recorded.

X-ray absorption fine structure (XAFS) measurement was performed using XAFCA beamline at the Singapore Synchrotron Light Source (SSLS) [62]. XAFS spectra were obtained in Sn L edge at room temperature.

Fourier-transform infrared spectroscopy (FTIR) measurement was done on Bruker Alpha II FTIR spectroscopy equipped with an ATR accessory in the range of 200-4000 cm^{-1}. Spectra were converted into absorbance by Bruker OPUS software.

Thermal gravimetric (TGA) measurement was performed on a TGA Q 500 instrument in the range of 25–800 °C with a ramping rate of 10 °C min^{-1} under a N_2 flow rate of 40 mL/min. 3 mg of each sample was used for TGA measurement.

Electrochemical impedance was done on a PARSTAT 3000 station with at three different frequencies (1.2 kHz, 2.4 kHz and 4.8 kHz) at a constant voltage of 0.5V. A traditional three electrode system was used, in which saturated Ag/AgCl electrode, Pt wire and a self-made electrode deposited with photocatalysts act as reference, counter and working electrodes respectively.

Photocatalysis Test

Photocatalytic hydrogen production from methanol was conducted in a 15 mL quartz bottle reactor with a silicone rubber septum under room temperature and atmospheric pressure. A 300 W Microsolar lamp (Beijing Perfect light Technology Co., Ltd) with an optical filter of AM 1.5 G was horizontally placed alongside the reactor. A certain amount of photocatalyst was added into the reactor while 90 min sonication was performed to disperse the photocatalysts in

10 mL alcohol (methanol/ethanol/iso-propanol). After that, the reactor was degassed by Ar gas for another 30 min to remove the residual air from the reactor. The products from the photocatalytic methanol decomposition were analysed by GC (Nexis 2030, Shimadzu Scientific instruments) which equipped with a thermal conductivity detector (TCD), and a flame ionization detector (FID) and a ShinCarbon (100/120, 1mm ID, 1/16″ OD) column. Before and after light irradiation, 50 µL of aliquot from the dead space of the reactor was taken out by a micro-syringe and manually injected into the GC, which then worked as references. Typically, the photocatalytic reaction was carried out for 4 h, while the irradiation time for stability test was varied between methanol, ethanol and iso-propanol. An Agilent 7890 A GC equipped with a FID and 7010 Triple Quadruple GC/MS/MS with helium as carrier gas were used to analyse the end products after photocatalytic reaction. Injections were split in 100:1 with a split flow of 150 mL/min and delivered through an autosampler. The inlet temperature was 220 ºC, while oven temperature was set in the range of 40-240 ºC, among which a ramping rate of 5 ºC/min was applied in the range of 40-100 ºC with no hold time and another ramping rate of 20 ºC/min used in the range of 100-240 ºC with a hole time of 3.5 min. Scans were measured from 10 mass to 300 mass using 300 ms scan time. The FID temperature was set to 250 ºC and the injection volume was 1 µL.

SUPPORTING INFORMATION

Supporting Information is available from the ACS Online Library or from the author.

ACKNOWLEDGEMENT

The authors gratefully acknowledge the support from the ANU Futures Scheme (Q4601024), the ANU Global Research Partnership Scheme (R468504649), ActewAGL Endowment Fund (Q4601028). MLC acknowledges an ARC Laureate Fellowship (FL170100041).

CONFLICT OF INTEREST

The authors declare no competing interests.

AUTHOR CONTRIBUTIONS

N. Uddin did the synthesis, all experiments, analysed the experimental data, and wrote the manuscript. Julien Langley and Dr. Nick Cox performed the EPR experiments, analyzed those experimental data and co-wrote the manuscript. Dr. Chao Zhang and Dr. Dmitri Golberg carried out the HR-TEM and EDX experiments and analysed those data. Dr. Haijao Lu optimized figures and tables and revised the manuscript and supporting information. Alfred Fung and Prof. Michelle Coote have analysed the reaction mechanism and its understandings. Dr. Xinmao Yin, Dr. Andrew T. S. Wee and Dr. Shibo Xi performed the XAFS studies and analysed those data. Zhichen Wan, Dr. Jingying Liu, and Prof. Qiaoling Bao have conducted a part of HR-TEM experiments and analysed those data. Dr. Hieu T. Nguyen performed the PL experiments. Dr. Zongyou Yin designed the whole idea for this work, outlined the expected experiments, analysed the experimental data, and co-wrote the paper. All of the authors discussed the results and reviewed the manuscript.

REFERENCES

(1) Fuss, S. The 1.5 °C target, political implications, and the role of BECCS. In: Oxford Research Encyclopedia, Climate Science. **2017,** 1–24, doi:10.1093/acrefore/9780190228620.013.585 (accessed Jan 1st, 2021).

(2) Rogelj, J.; Luderer, G.; Pietzcker, R. C.; Kriegler, E.; Schaeffer, M.; Krey, V.; Riahi, K. Energy system transformations for limiting end-of-century warming to below 1.5 °C. *Nat. Clim. Change.* **2015,** 5, 519-527.

(3) Minx, J. C.; Lamb, W. F.; Callaghan, M. W.; Bornmann, L.; Fuss, S. Fast growing research on negative emissions. *Environ. Res. Lett.* **2017,** 12, 035007.

(4) Albero, J.; Peng, Y.; García, H. Photocatalytic CO_2 Reduction to C2+ Products. *ACS Catal.* **2020,** 10, 5734-5749.

(5) Liu, J. Y.; Gong, X.-Q.; Li, R.; Shi, H.; Cronin, S. B.; Alexandrova, A. N. (Photo)Electrocatalytic CO_2 Reduction at the Defective Anatase TiO_2 (101) Surface. *ACS Catal.* **2020,** 10, 4048-4058.

(6) Goldemberg, J. World Energy Assessment: Energy and the challenge of sustainability. United Nations Development Programme, New York, NY, USA, **2000,** 135-171.

(7) Secretariat, R. Renewables 2012 global status report (Online), June 15, **2020,** 1-10. https://www.eqmagpro.com/wp-content/uploads/2020/06/gsr_2020_presentation_compressed-1-10.pdf (accessed Jan 1st, 2021).

(8) Creissen, C. E.; Fontecave, M. Solar-Driven Electrochemical CO_2 Reduction with Heterogeneous Catalysts. *Adv. Energy. Mater.* **2020,** 2002652.

(9) Yamaguchi, R.; Fujita, K.-i. Dehydrogenation catalyst, and carbonyl compound and hydrogen production method using said catalyst. U.S. Patents 9403159B2, August 2, **2016**.

(10) Xie, S.; Shen, Z.; Deng, J.; Guo, P.; Zhang, Q.; Zhang, H.; Ma, C.; Jiang, Z.; Cheng, J.; Deng, D. Visible light-driven C− H activation and C–C coupling of methanol into ethylene glycol. *Nat. Commun.* **2018,** 9, 1-7.

(11) Tan, H.; Kong, P.; Liu, M.; Gu, X.; Zheng, Z. Enhanced photocatalytic hydrogen production from aqueous-phase methanol reforming over cyano-carboxylic bifunctionally-modified carbon nitride. *Chem. Commun.* **2019,** 55, 12503-12506.

(12) Lin, L.; Zhou, W.; Gao, R.; Yao, S.; Zhang, X.; Xu, W.; Zheng, S.; Jiang, Z.; Yu, Q.; Li, Y. W. Low-temperature hydrogen production from water and methanol using Pt/α-MoC catalysts. *Nature* **2017,** 544, 80-83.

(13) Fang, S.; Sun, Z.; Hu, Y. H. Insights into the Thermo-Photo Catalytic Production of Hydrogen from Water on a Low-Cost NiO_x-Loaded TiO_2 Catalyst. *ACS Catal.* **2019,** 9, 5047-5056.

(14) González-Cobos, J.; Rico, V. J.; González-Elipe, A. n. R.; Valverde, J. L.; de Lucas-Consuegra, A. Electrocatalytic System for the Simultaneous Hydrogen Production and Storage from Methanol. *ACS Catal.* **2016,** 6, 1942-1951.

(15) Chao, Y.; Zhang, W.; Wu, X.; Gong, N.; Bi, Z.; Li, Y.; Zheng, J.; Zhu, Z.; Tan, Y. Visible-light direct conversion of ethanol to 1, 1-Diethoxyethane and hydrogen over a non-precious metal photocatalyst. *Chem. Eur. J.* **2019,** 25, 189-194.

(16) Chao, Y.; Lai, J.; Yang, Y.; Zhou, P.; Zhang, Y.; Mu, Z.; Li, S.; Zheng, J.; Zhu, Z.; Tan, Y. Visible light-driven methanol dehydrogenation and conversion into 1, 1-dimethoxymethane over a non-noble metal photocatalyst under acidic conditions. *Catal. Sci. Technol.* **2018,** 8, 3372-3378.

(17) Chai, Z.; Zeng, T. T.; Li, Q.; Lu, L. Q.; Xiao, W. J.; Xu, D. Efficient Visible Light-Driven Splitting of Alcohols into Hydrogen and Corresponding Carbonyl Compounds over a Ni-Modified CdS Photocatalyst. *J. Am. Chem. Soc.* **2016,** 138, 10128-10131.

(18) Nielsen, M.; Alberico, E.; Baumann, W.; Drexler, H.-J.; Junge, H.; Gladiali, S.; Beller, M. Low-temperature aqueous-phase methanol dehydrogenation to hydrogen and carbon dioxide. *Nature* **2013,** 495, 85-89.

(19) Fujita, K. i.; Kawahara, R.; Aikawa, T.; Yamaguchi, R. Hydrogen Production from a Methanol–Water Solution Catalyzed by an Anionic Iridium Complex Bearing a Functional Bipyridonate Ligand under Weakly Basic Conditions. *Angew. Chem. Int. Ed.* **2015,** 54, 9057-9060.

(20) Alberico, E.; Lennox, A. J.; Vogt, L. K.; Jiao, H.; Baumann, W.; Drexler, H.-J.; Nielsen, M.; Spannenberg, A.; Checinski, M. P.; Junge, H. Unravelling the mechanism of basic aqueous methanol dehydrogenation catalyzed by Ru–PNP pincer complexes. *J. Am. Chem. Soc.* **2016,** 138, 14890-14904.

(21) Kuo, H. L.; Kuo, C. Y.; Liu, C. H.; Chao, J. H.; Lin, C. H. A highly active bi-crystalline photocatalyst consisting of TiO_2 (B) nanotube and anatase particle for producing H_2 gas from neat ethanol. *Catal. Lett.* **2007,** 113, 7-12.

(22) Nadeem, M.; Murdoch, M.; Waterhouse, G.; Metson, J.; Keane, M.; Llorca, J.; Idriss, H. Photoreaction of ethanol on Au/TiO_2 anatase: comparing the micro to nanoparticle size activities of the support for hydrogen production. *J. Photochem. Photobiol. A* **2010,** 216, 250-255.

(23) Ampelli, C.; Passalacqua, R.; Genovese, C.; Perathoner, S.; Centi, G.; Montini, T.; Gombac, V.; Jaen, J. J. D.; Fornasiero, P. H_2 production by selective photo-dehydrogenation of ethanol in gas and liquid phase on CuO_x/TiO_2 nanocomposites. *RSC Adv.* **2013,** 3, 21776-21788.

(24) Zhang, Y.; Xia, B.; Ran, J.; Davey, K.; Qiao, S. Z. Atomic-Level Reactive Sites for Semiconductor-Based Photocatalytic CO_2 Reduction. *Adv. Energy Mater.* **2020,** 10, 1903879.

(25) Liu, Y.; Yang, S.; Yin, S. N.; Feng, L.; Zang, Y.; Xue, H. In situ construction of fibrous AgNPs/g-C_3N_4 aerogel toward light-driven CO_x-free methanol dehydrogenation at room temperature. *Chem. Eng. J.* **2018,** 334, 2401-2407.

(26) Zhang, Q.; Du, C.; Zhao, Q.; Zhou, C.; Yang, S. Visible light-driven the splitting of ethanol into hydrogen and acetaldehyde catalyzed by fibrous AgNPs/CdS hybrids at room temperature. *J. Taiwan Inst. Chem. Eng.* **2019,** 102, 182-189.

(27) Lin, C. H.; Chao, J. H.; Tsai, W. J.; He, M. J.; Chiang, T. J. Effects of electron charge density and particle size of alkali metal titanate nanotube-supported Pt photocatalysts on production of H_2 from neat alcohol. *Phys. Chem. Chem. Phys.* **2014,** 16, 23743-23753.

(28) Gazsi, A.; Schubert, G.; Bánsági, T.; Solymosi, F. Photocatalytic decompositions of methanol and ethanol on Au supported by pure or N-doped TiO_2. *J. Photochem. Photobiol. A* **2013,** 271, 45-55.

(29) Liu, Z.; Yin, Z.; Cox, C.; Bosman, M.; Qian, X.; Li, N.; Zhao, H.; Du, Y.; Li, J.; Nocera, D. G. Room temperature stable CO_x-free H_2 production from methanol with magnesium oxide nanophotocatalysts. *Sci. Adv.* **2016,** 2, e1501425.

(30) Pang, Y.; Uddin, M. N.; Chen, W.; Javaid, S.; Barker, E.; Li, Y.; Suvorova, A.; Saunders, M.; Yin, Z.; Jia, G. Colloidal Single-Layer Photocatalysts for Methanol-Storable Solar H_2 Fuel. *Adv. Mater.* **2019,** 31, 1905540.

(31) Liu, Y. N.; Shen, C. C.; Jiang, N.; Zhao, Z. W.; Zhou, X.; Zhao, S. J.; Xu, A. W. g-C_3N_4 Hydrogen-Bonding Viologen for Significantly Enhanced Visible-Light Photocatalytic H_2 Evolution. *ACS Catal.* **2017,** 7, 8228-8234.

(32) Shiraishi, Y.; Kanazawa, S.; Sugano, Y.; Tsukamoto, D.; Sakamoto, H.; Ichikawa, S.; Hirai, T. Highly Selective Production of Hydrogen Peroxide on Graphitic Carbon Nitride (g-C_3N_4) Photocatalyst Activated by Visible Light. *ACS Catal.* **2014,** 4, 774-780.

(33) Jiang, W.; Zong, X.; An, L.; Hua, S.; Miao, X.; Luan, S.; Wen, Y.; Tao, F. F.; Sun, Z. Consciously Constructing Heterojunction or Direct Z-Scheme Photocatalysts by Regulating Electron Flow Direction. *ACS Catal.* **2018,** 8, 2209-2217.

(34) Su, T.; Shao, Q.; Qin, Z.; Guo, Z.; Wu, Z. Role of Interfaces in Two-Dimensional Photocatalyst for Water Splitting. *ACS Catal.* **2018,** 8 (3), 2253-2276.

(35) Jannat, A.; Haque, F.; Xu, K.; Zhou, C.; Zhang, B. Y.; Syed, N.; Mohiuddin, M.; Messalea, K. A.; Li, X.; Gras, S. L.; Wen, X.; Fei, Z.; Haque, E.; Walia, S.; Daeneke, T.; Zavabeti, A.; Ou, J. Z. Exciton-Driven Chemical Sensors Based on Excitation-Dependent Photoluminescent Two-Dimensional SnS. *ACS Appl. Mater. Interfaces.* **2019,** 11, 42462-42468.

(36) Fina, F.; Callear, S. K.; Carins, G. M.; Irvine, J. T. Structural investigation of graphitic carbon nitride via XRD and neutron diffraction. *Chem. Mater.* **2015,** 27, 2612-2618.

(37) Kobylinski, M. M.; Ruhmlieb, C.; Kornowski, A.; Mews, A. Hexagonally Shaped Two-Dimensional Tin (II) sulfide Nanosheets: Growth Model and Controlled Structure Formation. *J. Phys. Chem. C* **2018,** 122, 5784-5795.

(38) Qiu, F.; Li, W.; Wang, F.; Li, H.; Liu, X.; Sun, J. In-situ synthesis of novel Z-scheme SnS_2/BiOBr photocatalysts with superior photocatalytic efficiency under visible light. *J. Colloid Interface Sci.* **2017,** 493, 1-9.

(39) Zhu, A.; Qiao, L.; Jia, Z.; Tan, P.; Liu, Y.; Ma, Y.; Pan, J. C–S bond induced ultrafine SnS_2 dot/porous g-C_3N_4 sheet 0D/2D heterojunction: synthesis and photocatalytic mechanism investigation. *Dalton Trans.* **2017,** 46, 17032-17040.

(40) Castner, D. G.; Hinds, K.; Grainger, D. W. X-ray photoelectron spectroscopy sulfur 2p study of organic thiol and disulfide binding interactions with gold surfaces. *Langmuir* **1996,** 12, 5083-5086.

(41) Jia, T.; Fu, F.; Li, J.; Deng, Z.; Long, F.; Yu, D.; Cui, Q.; Wang, W. Rational construction of direct Z-scheme SnS/g-C_3N_4 hybrid photocatalyst for significant enhancement of visible-light photocatalytic activity. *Appl. Surf. Sci.* **2020,** 499, 143941.

(42) Miller, T.; Jorge, A. B.; Suter, T.; Sella, A.; Cora, F.; McMillan, P. Carbon nitrides: synthesis and characterization of a new class of functional materials. *Phys. Chem. Chem. Phys.* **2017,** 19, 15613-15638.

(43) Cao, S.; Low, J.; Yu, J.; Jaroniec, M. Polymeric photocatalysts based on graphitic carbon nitride. *Adv. Mater.* **2015,** 27, 2150-2176.

(44) Liu, H.; Zhang, Y.; Li, R.; Sun, X.; Désilets, S.; Abou-Rachid, H.; Jaidann, M.; Lussier, L.-S. Structural and morphological control of aligned nitrogen-doped carbon nanotubes. *Carbon* **2010,** 48, 1498-1507.

(45) Liu, Z.; Handa, K.; Kaibuchi, K.; Tanaka, Y.; Kawai, J. Comparison of the Sn L edge X-ray absorption spectra and the corresponding electronic structure in Sn, SnO, and SnO_2. *J Electron Spectros Relat Phenomena*. **2004,** 135, 155-158.

(46) Balouch, A.; Ali Umar, A.; Shah, A. A.; Mat Salleh, M.; Oyama, M. Efficient heterogeneous catalytic hydrogenation of acetone to isopropanol on semihollow and porous palladium nanocatalyst. *ACS Appl. Mater. Interfaces* **2013,** 5, 9843-9849.

(47) Matsumura, Y.; Tanaka, K.; Tode, N.; Yazawa, T.; Haruta, M. Catalytic methanol decomposition to carbon monoxide and hydrogen over nickel supported on silica. *J. Mol. Catal. A Chem.* **2000,** 152, 157-165.

(48) Zhang, B.; Tang, X.; Li, Y.; Xu, Y.; Shen, W. Hydrogen production from steam reforming of ethanol and glycerol over ceria-supported metal catalysts. *Int. J. Hydrog. Energy* **2007,** 32, 2367-2373.

(49) Sexton, B. A.; Rendulic, K. D.; Huges, A. E. Decomposition pathways of C_1-C_4 alcohols adsorbed on platinum (111). *Surf. Sci.* **1982,** 121, 181-198.

(50) Liu, G.; Zhao, G.; Zhou, W.; Liu, Y.; Pang, H.; Zhang, H.; Hao, D.; Meng, X.; Li, P.; Kako, T. In situ bond modulation of graphitic carbon nitride to construct p–n homojunctions for enhanced photocatalytic hydrogen production. *Adv. Funct. Mater.* **2016,** 26, 6822-6829.

(51) Gelderman, K.; Lee, L.; Donne, S. Flat-band potential of a semiconductor: using the Mott–Schottky equation. *J. Chem. Educ.* **2007,** 84, 685.

(52) Low, J.; Jiang, C.; Cheng, B.; Wageh, S.; Al-Ghamdi, A. A.; Yu, J. A review of direct Z-scheme photocatalysts. *Small Methods* **2017,** 1, 1700080.

(53) Lee, C.-H.; Lee, G.-H.; Van Der Zande, A. M.; Chen, W.; Li, Y.; Han, M.; Cui, X.; Arefe, G.; Nuckolls, C.; Heinz, T. F. Atomically thin p–n junctions with van der Waals heterointerfaces. *Nat. Nanotechnol.* **2014,** 9, 676.

(54) Stoll, S.; Schweiger, A. EasySpin, a comprehensive software package for spectral simulation and analysis in EPR. *J. Magn. Reson.* **2006,** 178, 42-55.

(55) Zhang, L. J.; Li, S.; Liu, B. K.; Wang, D. J.; Xie, T. F. Highly efficient CdS/WO_3 photocatalysts: Z-scheme photocatalytic mechanism for their enhanced photocatalytic H_2 evolution under visible light. *ACS Catal.* **2014,** 4, 3724-3729.

(56) Bhattacharyya, K.; Tripathi, A. K.; Gupta, N. M.; Tyagi, A. K. Photodegradation of Methanol Under UV–Visible Irradiation by Titania Dispersed on Polyester Cloth. *Photochem. Photobiol.* **2010,** 86, 241-246.

(57) Fischer, I. High-resolution photoelectron-spectroscopy of radicals. *Int. J. Mass Spectrom.* **2002,** 216, 131-153.

(58) Petraco, N. D. K.; Allen, W. D.; III, H. F. S. Fragmentation path for hydrogen atom dissociation from methoxy radical. *J. Chem. Phys.* **2002,** 116, 10229-10237.

(59) SaeboØ, S.; Radom, L.; III, H. F. S. The weakly exothermic rearrangement of methoxy radical ($CH_3O\cdot$) to the hydroxymethyl radical ($CH_2OH\cdot$). *J. Chem. Phys.* **1983,** 78, 845-853.
(60) Ralston, K. J.; Hulme, A. N. The Evans–Tishchenko Reaction: Scope and Applications. *Synthesis* **2012,** 44, 2310-2324.
(61) Wuts, P. G. M.; Greene, T. W. Greene's protective groups in organic synthesis-Protection for the Carbonyl Group (Chapter 4); John Wiley & Sons, Inc., Publication: Hoboken, NJ, **2006,** 431-532.
(62) Du, Y.; Zhu, Y.; Xi, S.; Yang, P.; Moser, H. O.; Breese, M. B.; Borgna, A. XAFCA: a new XAFS beamline for catalysis research. *J. Synchrotron Radiat.* **2015,** 22, 839-843.